Radiative conductivity and abundance of post-perovskite in the lowermost mantle

Sergey S. Lobanov [a,b,*,1], Nicholas Holtgrewe [a,c,1], Jung-Fu Lin [d,e],
Alexander F. Goncharov [a,f]

[a] *Geophysical Laboratory, Carnegie Institution of Washington, Washington, DC 20015, USA*
[b] *Sobolev Institute of Geology and Mineralogy, Siberian Branch Russian Academy of Sciences, Novosibirsk 630090, Russia*
[c] *Howard University, 2400 Sixth Street NW, Washington, DC 20059, USA*
[d] *Department of Geological Sciences, Jackson School of Geosciences, The University of Texas at Austin, Austin, TX 78712, USA*
[e] *Center for High Pressure Science and Technology Advanced Research (HPSTAR), Shanghai 130012, China*
[f] *Key Laboratory of Materials Physics, Institute of Solid State Physics CAS, Hefei 230031, China*

A B S T R A C T

Thermal conductivity of the lowermost mantle governs the heat flow out of the core energizing planetary-scale geological processes. Yet, there are no direct experimental measurements of thermal conductivity at relevant pressure–temperature conditions of Earth's core–mantle boundary. Here we determine the radiative conductivity of post-perovskite at near core–mantle boundary conditions by optical absorption measurements in a laser-heated diamond anvil cell. Our results show that the radiative conductivity of $Mg_{0.9}Fe_{0.1}SiO_3$ post-perovskite ($\sim$1.1 W/m/K) is almost two times smaller than that of bridgmanite ($\sim$2.0 W/m/K) at the base of the mantle. By combining this result with the present-day core–mantle heat flow and available estimations on the lattice thermal conductivity we conclude that post-perovskite is at least as abundant as bridgmanite in the lowermost mantle which has profound implications for the dynamics of the deep Earth.

© 2017 Elsevier B.V. All rights reserved.

1. Introduction

The lowermost 200–400 km of the mantle is a critical region responsible for the core–mantle interaction powering all major geological processes on Earth (Lay et al., 2008). Specifically, thermal conductivity of the thermal boundary layer (TBL) above the core–mantle boundary (CMB) determines the heat flow out of the core that provides energy to sustain the mantle global circulation and to drive the geodynamo (Lay et al., 2008). Seismic structures of the lowermost mantle, however, are complex (Lay et al., 2006; van der Hilst et al., 2007) implying that the thermal conductivity of the region is non-uniform due to variations in chemical (e.g. iron) and/or mineralogical contents as well as texturing of the constituting minerals. The nature of the seismic heterogeneity near the CMB, including a sharp increase in shear wave velocity and anti-correlations of seismic parameters,

has been linked to the bridgmanite (Bdgm) to post-perovskite (Ppv) transition (Murakami et al., 2004; Oganov and Ono, 2004), as these phases have contrasting elastic, rheological, and transport properties (Oganov and Ono, 2004). Indeed, measurements and computations of lattice thermal conductivity (k_{lat}) in Bdgm and Ppv have revealed that Ppv conducts heat 50–60% more efficiently than Bdgm (Ammann et al., 2014; Haigis et al., 2012; Ohta et al., 2012), suggesting that the distribution of the Ppv phase can significantly enhance the heat flux out of the core. However, no mineral physics constraints are available on the radiative thermal conductivity (k_{rad}) of Ppv, which should play an increasingly important role at high temperature (Hofmeister, 2014), as well as on the Ppv abundance in the lowermost mantle. This has hampered our understanding of how the heat flux across the CMB may vary laterally and what magnitude of the energy source in the mantle and the outer core is needed to power their convections.

Previous estimates of radiative thermal conductivity at lower mantle conditions were based on high-pressure room-temperature measurements of the absorption coefficients of representative minerals in the mid/near-infrared and visible spectral range (Goncharov et al., 2006, 2008, 2009, 2015; Keppler et al., 2008). The presence of an intense thermal radiation emitted from the hot sample

* Corresponding author at: Geophysical Laboratory, Carnegie Institution of Washington, Washington, DC 20015, USA.
E-mail addresses: slobanov@carnegiescience.edu, slobanov@igm.nsc.ru (S.S. Lobanov).
[1] These authors contributed equally to this work.

makes measurements of the optical properties at high temperatures relevant to the lowermost mantle (approximately 3000 K) very challenging as common light sources have similar radiative temperatures. In the absence of the experimental data, the effect of temperature was neglected. It has been argued that temperature-induced variations in the absorption spectrum of Bdgm are small as intensity of the crystal-field band is determined by a symmetry distortion of the $Fe^{2+}O_{12}$-polyhedra in Bdgm (Keppler et al., 2008). However, the intensity of the crystal field spectrum in iron-bearing minerals can be sensitive to pressure, temperature, iron concentration, and iron spin states (Burns, 1993; Goncharov et al., 2006, 2010; Keppler et al., 2007; Lobanov et al., 2015, 2016, 2017). Moreover, due to a substantial amount of Fe^{3+} in Bdgm and Ppv at lower mantle conditions (Sinmyo et al., 2006), the absorption coefficients and thus the radiative conductivity of these minerals are also governed by the Fe^{2+}–Fe^{3+} charge transfer (CT) (Burns, 1993), which is expected to diminish with temperature (Mattson and Rossman, 1987). Therefore, to ascertain the presently unknown radiative conductivity of iron-bearing minerals at expected CMB conditions, it is of fundamental importance to underpin physical mechanisms that govern optical absorption of lower mantle minerals at simultaneous high pressure–temperature conditions. It is also desirable to assess the intensity of the absorption bands as a function of the total iron content because the solubility of iron in lower mantle minerals can vary with pressure, temperature, and phase/spin transitions (Ismailova et al., 2016).

2. Experimental methods

2.1. Absorption measurements in the visible (13000–22000 cm^{-1}) and near-infrared ranges (6200–11000 cm^{-1}) were divided into heating runs at two laser-heating systems equipped with different spectrometers and detectors (denoted hereafter as VIS and IR runs). A Leukos Pegasus pulsed supercontinuum light source (400–2400 nm) was inserted into the optical path of both systems, serving as a probe. For the VIS, the transmitted probe light was collected using a spectrometer with a 300 gr/mm grating and 300 mm focal length and a gated iCCD detector (Andor iStar SR-303i-A) synchronized with the supercontinuum pulses, identically to that described in Lobanov et al. (2016). For the IR, we used Action Spectra Pro 2300i spectrometer equipped with a 150 gr/mm grating and an ungated InGaAs detector (Princeton Instruments Model 7498-0001). The collection of 2500 supercontinuum pulses over 10 ms was initiated 200 ms after the start of the 1 s laser heating. The large number of bright probe pulses in a short accumulation window was important to increase signal-to-noise ratio and suppress thermal background. Absorption coefficient at high temperature (T) was evaluated as $\alpha(\upsilon) = \ln(10) * \frac{1}{d} * (-\log_{10}(\frac{I_{sample}^{T} - Bckg^{T}}{I_{reference}^{300\ K} - Bckg^{300\ K}}))$, where d is the sample thickness, I_{sample}^{T} is the intensity of light transmitted through the sample at T, $I_{reference}^{300\ K}$ is the intensity of light through the pressure medium at 300 K, $Bckg^{T}$ is background at T, and $Bckg^{300\ K}$ is background at 300 K. Reflections from the sample-medium interface were neglected as these are typically small ($<2\%$) in the frequency range of interest (Goncharov et al., 2009). Background at high T was collected right after the high T absorption measurement at identical laser-heating power and timing setup. The gap in absorption coefficients at ~9000–10500 cm^{-1} is due to the filters used to block the 1070 nm heating pulse, while the gap at 11000–13000 cm^{-1} is due to the limited sensitivity of the iCCD and InGaAs detectors. The sample absorbance in these ranges was extrapolated based on the room temperature data collected with a conventional light source. The 2500–6200 cm^{-1} region was extrapolated in a similar way and assumed temperature-independent

as it is essentially featureless. Below 2500 cm^{-1}, a strong absorption due to phonons (fundamentals and overtones) is not expected to change substantially with temperature (Thomas et al., 2012); thus, this region does not contribute significantly to the radiative conductivity and was excluded from the integration. Likewise, we excluded the range above 25000 cm^{-1} where the Planck function is essentially zero at all temperatures of interest.

2.2. Double-sided laser-heating and temperature measurements in the VIS runs were identical to that of Lobanov et al. (2016). For the IR runs, at double-sided laser-heating we could only perform single-sided temperature measurements for which the grating was centered at 1320 nm and the supercontinuum was blocked. In both VIS and IR, temperatures measurements were taken before and after the corresponding collection of the absorbance data at an identical laser power. The laser power was optimized to achieve comparable temperatures in the VIS and IR runs (within 50–100 K). Optical responses of the VIS and IR systems were calibrated using a standard white lamp (Optronics Laboratories OL 220C). To extract the temperature, the emission spectra were fitted to the Planck black body function using the T-Rax software (C. Prescher). The reported temperature is an average of the VIS and IR measurements.

2.3. Sample thickness required to deduce the absorption coefficient of $Mg_{0.6}Fe_{0.4}SiO_3$–Ppv was determined via white light interferometry at 130 GPa through the NaCl pressure medium (3.6 µm). Additionally, the sample thickness was confirmed by direct SEM imaging of the recovered sample at 1 atm (~5 µm). The difference in sample thickness between the two estimates is the main source of uncertainty in k_{rad} (~25%). Other contributions to the uncertainty include ambiguities in the refractive index of Ppv at high pressure, and to a lesser extent, high temperature (~1%/1000 K Ruf et al., 2000).

3. Results and discussion

In this work we have studied optical properties of iron-rich, Fe^{3+}-bearing Ppv ($Mg_{0.6}Fe_{0.4}SiO_3$) at 300–2050 K and 130 GPa using laser-heated diamond anvil cells combined with a pulsed ultra-bright supercontinuum probe (400–2400 nm) synchronized with the collection windows of gated visible and infrared detectors. The latter allowed diminishing the contribution of thermal radiation to the optical signal at high temperature by several orders of magnitude. We determined quantitatively the reduction in intensity of all Ppv absorption bands in the visible-infrared range at high pressure and temperature. These, in turn, have allowed us to constrain the spin and valence states of iron in Ppv and its radiative conductivity at expected CMB conditions. Combined with literature data on the absorption coefficients of Bdgm and ferropericlase (Fp), these results enable us to construct a radiative thermal conductivity model for the lowermost mantle in order to address the CMB heat flux and Ppv content in the region.

Iron-rich ($Mg_{0.6}Fe_{0.4}SiO_3$) Ppv was synthesized in a diamond anvil cell using enstatite powder of the corresponding composition sandwiched between NaCl layers, similar to procedures used in previous reports on the spin and valence states in Ppv (Lin et al., 2008). The sample was compressed to 130 GPa at room temperature and then laser-heated at 2500–2800 K for 6–8 hr at 13IDD beamline of GSECARS, Advanced Photon Source. To avoid chemical segregation upon laser-heating, the hot spot was moved during the process. Synthesis was confirmed by synchrotron x-ray diffraction that showed a complete transformation to the Ppv phase (Supplementary Fig. S1). However, several weak unindexed peaks suggest that the sample is not homogeneous and contains minor impurities. After successful synthesis of Ppv, analysis of the measured room-temperature absorption spectrum in the 6000–22500 cm^{-1}
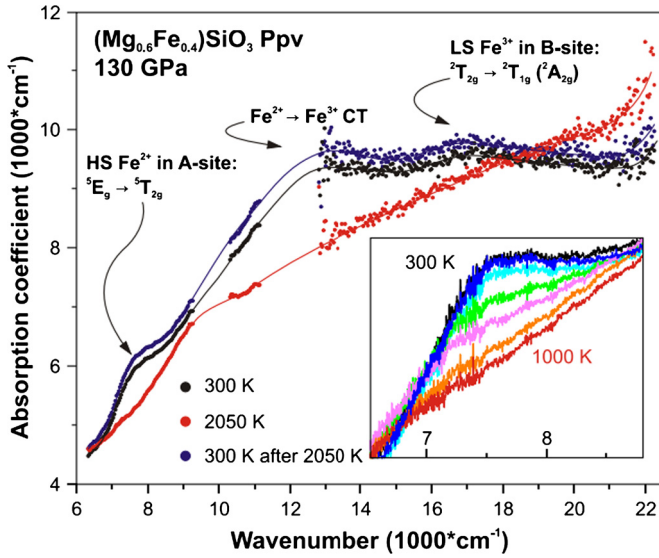
Fig. 1. Absorption coefficients of Ppv with $Mg_{0.6}Fe_{0.4}SiO_3$ composition at 130 GPa. Black: before heating; red: at ∼ 2050 K; blue: quenched to room temperature. Spectral regions that lack absorbance data are due to the need to block the spectral range (9500–10500 cm^{-1}) near the heating laser wavelength (1070 nm) and the limited sensitivity of the iCCD and InGaAs detectors at 11000–13000 cm^{-1}. Lines are fits to the spectra to guide the eye. Inset: temperature-induced changes in the 6500–8700 cm^{-1} range at $T = 300$ (black and dark blue) to ∼ 1000 K (red). All observed transformations are reversible. (For interpretation of the references to color in this figure legend, the reader is referred to the web version of this article.)

range shows three distinct features at energies typical for crystal field and CT transitions (Fig. 1) (Burns, 1993).

The band assignment of our absorption spectra is based on first-principles calculations at zero Kelvin (Hsu et al., 2012; Yu et al., 2012) and is consistent with experimental room-temperature Mössbauer data collected previously on samples with similar synthesis conditions (Lin et al., 2008), providing necessary reference information on the identification for the iron spin and valence states in Ppv at 300 K (see Supplementary Materials). Specifically, low spin (LS) Fe^{3+} occupies the 6-fold B-site (Supplementary Fig. S2), while the 8-fold A-site is occupied by both high spin (HS) Fe^{3+} and HS Fe^{2+}. Combining these results with Tanabe–Sugano diagrams for d^5 and d^6 elements we deduce the spin-allowed electronic transitions in the crystal field of iron in Ppv at 130 GPa and 300 K: $^5E_g \rightarrow {}^5T_{2g}$ in A-site HS Fe^{2+} and $^2T_{2g} \rightarrow {}^2T_{1g}$ ($^2A_{2g}$) in B-site LS Fe^{3+}. Importantly, all crystal field transitions in HS Fe^{3+} are spin-forbidden.

The band centered at ∼7500 cm^{-1} is assigned to the $^5E_g \rightarrow {}^5T_{2g}$ transition in HS Fe^{2+} at the A-site based on the relatively weak crystal field splitting energy of its 8-fold coordination (see Supplementary Materials). Upon laser-heating, the $^5E_g \rightarrow {}^5T_{2g}$ band red-shifts and weakens continuously with increasing temperature to T ∼ 1000 K (Fig. 1). Interestingly, the red-shift represents a typical behavior of a crystal field band due to the thermal expansion decreasing the crystal field splitting energy. The vanishing intensity, however, is highly uncommon for single-ion crystal field bands (Burns, 1993). Likewise, the band intensity at 300 K is not scaled linearly with the Ppv iron content (Supplementary Fig. S3), as would be expected for single-ion crystal field bands, suggesting that the absorption of light by the A-site HS Fe^{2+} is enhanced by interactions with the edge-sharing B-site Fe^{3+}. Indeed, exchange-coupling interactions of adjacent transition metal ions have been employed to explain the anomalous temperature and concentration behavior of the crystal field bands (e.g. Ferguson et al., 1965). However, the importance of this transition mechanism for the absorption coefficient of lower mantle minerals has been previously over-

looked. Alternatively, the disappearance of the band at $T \sim 1000$ K may indicate that the $^5E_g \rightarrow {}^5T_{2g}$ band becomes parity-forbidden due to temperature-induced static and/or dynamic distortions imposing a center of symmetry to the A-site (vibronic decoupling) (Burns, 1993). A detailed crystallographic analysis of intensities and positions of multigrain Bragg reflections may allow discriminating between these two hypotheses. In the absence of such information we assume the exchange-coupled mechanism plays a dominant role in the intensity weakening.

The band centered at 17500 cm^{-1} is assigned to the $^2T_{2g} \rightarrow {}^2T_{1g}$ ($^2A_{2g}$) transition in LS Fe^{3+} at the B-site (Lobanov et al., 2017) as it corresponds to the lowest energy spin-allowed excited state of d^5 elements (Supplementary Fig. S4 and Supplementary Materials). At 2050 K, the LS Fe^{3+} band is no longer observed (Fig. 1), indicating a temperature-induced LS to HS transition at expected P–T conditions of the CMB. In Al-bearing Bdgm all iron is likely accommodated by the 12-folded A-site and remain in the HS state at lower mantle P–T (Lin et al., 2016), as opposed to Fp which may contain a significant portion of LS iron (up to 50%) at the bottom of the lower mantle (Holmstrom and Stixrude, 2015). Accordingly, Fp is the only major host of LS iron in the lower mantle.

The most prominent spectral feature observed here is the broad absorption band at 12000–13000 cm^{-1} (Fig. 1) which we assign to a Fe^{2+}–Fe^{3+} CT transition. This band is characteristic of mixed-valence compounds (Burns, 1993) and has an increased bandwidth compared to crystal field bands (Mattson and Rossman, 1987). The decreased intensity at high temperature supports this assignment because the number of absorbing Fe^{2+}–Fe^{3+} pairs in the ground state (N) decreases with temperature (T) as $N \sim 1 - \exp(-E_a/kT)$, where E_a is the activation energy for a thermally-induced CT, which may be as low as 1000–4000 cm^{-1} (Sherman, 1987), and k is the Boltzmann constant. Other mechanisms may also be used to explain the reduced intensity of this band at 2050 K such as the temperature-inhibited ferromagnetic interaction in the Fe^{2+}–Fe^{3+} pair (Cox, 1980). Aside the Fe^{2+}–Fe^{3+} CT, Fe^{2+}–O and Fe^{3+}–O CT (absorption edge) may give rise to the intense absorption in the spectrum at frequencies above 22000 cm^{-1} (Fig. 1; Supplementary Fig. S3).

The observed temperature-induced changes in Ppv optical absorbance are fully reversible and have also been confirmed in Ppv25 ($Mg_{0.75}Fe_{0.25}SiO_3$), which was prepared similarly to Ppv 40 (Supplementary Fig. S5). Therefore, the transformations in the absorption coefficient of Ppv40 at 2050 K are characteristic of Ppv and can be used to address the radiative conductivity of lower mantle Ppv, which likely has a lower total iron content. A conventional approach to assess k_{rad} for a given room temperature absorption coefficient (α) is:

$$k_{rad}(T) = \frac{4n^2}{3} \int_0^\infty \frac{1}{\alpha(\nu)} \frac{\partial I(\nu, T)}{\partial T} d\nu \qquad (1)$$

where n is the refractive index of a given mineral, ν is frequency, and $I(\nu, T)$ is the Planck function (Goncharov et al., 2008; Keppler et al., 2008). As revealed in this study, the absorption coefficient of Ppv is controlled by a number of physical mechanisms such as the temperature-activated spectroscopic selection rules and temperature-inhibited magnetic coupling. It follows that most accurate values of k_{rad} require absorption coefficients evaluated at high temperature. Unlike previous studies of lower mantle k_{rad} (Goncharov et al., 2006, 2008, 2009, 2015; Keppler et al., 2008), we determined the efficiency of the radiative heat transfer mechanism at high temperature based on the 2050 K absorption data. The comparison based on the 300 and 2050 K data reveals that the effect of temperature-dependent absorption coefficient on k_{rad} is on the order of 7% (Fig. 2), in spite of the substantial changes
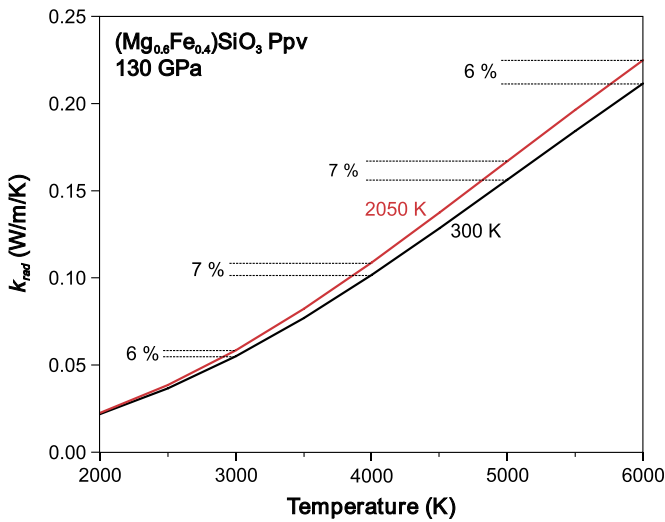
Fig. 2. Radiative thermal conductivity of $Mg_{0.6}Fe_{0.4}SiO_3$–Ppv at 130 GPa evaluated using absorption coefficients shown in Fig. 1 for different sample temperatures. The difference in k_{rad} evaluated from the absorption spectrum at 2050 K is 6–7% higher than that evaluated from the spectra at 300 K.

Fig. 3. Radiative thermal conductivity (k_{rad}) of Ppv (dark blue) and Bdgm (black) with $Mg_{0.9}Fe_{0.1}SiO_3$ composition and Fp ($Mg_{0.9}Fe_{0.1}O$) in the thermal boundary layer (TBL) along the intermediate geotherm of van der Hilst et al. (2007). k_{rad} of Ppv was calculated using its absorption coefficient at 130 GPa reported by Goncharov et al. (2010) within the conventional formula (e.g. Goncharov et al., 2008) and then corrected ($k_{rad} * 1.07$) for high temperature effects on the absorption coefficient. Pressure-dependence was neglected as it is weak over the relatively small pressure range of TBL. The overall uncertainty in k_{rad} is ~25% due to the ambiguity in the refractive index and sample thickness of Ppv. k_{rad} of Bdgm is based on the spectrum at 133 GPa and 300 K reported by Goncharov et al. (2008) and was corrected for high-temperature effects ($k_{rad} * 1.07$). k_{rad} of Fp, $(Mg_{0.85}Fe_{0.15})O$, (green) is calculated based on the room-temperature spectrum at 133 GPa (Goncharov et al., 2009) and is not corrected for temperature effects. The red curve is the Hashin–Shtrikman averaged (Hashin and Shtrikman, 1962) k_{rad} of 0.8 Bdgm or Ppv, and 0.2 Fp by volume. The kinked form of the red curve is due to the presumed 'double-crossing' (Hernlund et al., 2005) in the Ppv lens (gray area) assuming a temperature gradient of 7 K/km and a CMB temperature of 3950 K. Inset: radiative conductivity of $Mg_{1-x}Fe_xSiO_3$–Ppv for $x = 0.1$ (dark blue), $x = 0.2$ (orange), and $x = 0.3$ (red), respectively at 130 GPa. Blue-colored area shows the 7% upward correction due to the temperature-dependent absorption coefficient. (For interpretation of the references to color in this figure, the reader is referred to the web version of this article.)

in the absorption spectra (Fig. 1). The relative difference is maximal at 3500–5500 K due to the maximum overlap of the blackbody radiation with temperature-depressed absorption coefficient (Supplementary Fig. S6). As the refractive index of Ppv at 130 GPa is unknown, we assume a wavelength- and temperature-independent value of $n = 2.1$, based on a density-corrected refractive index of Bdgm (Wall et al., 1986). We estimated a combined uncertainty of ~25% in k_{rad} due to uncertainties in determination of both sample thickness and refractive index (see methods).

The radiative conductivity of the lowermost mantle is determined by absorption coefficients of its constituting materials likely including Ppv, Bdgm, and Fp. In turn, absorption coefficients of these phases strongly depend on their iron content. The Ppv composition studied here ($Mg_{0.6}Fe_{0.4}SiO_3$) is not representative of pyrolite (Fe/(Fe + Mg) ~0.1). Accordingly, to construct a model of radiative conductivity in the TBL we used previously reported room-temperature absorption coefficients of Ppv ($Mg_{0.9}Fe_{0.1}SiO_3$) (Goncharov et al., 2010), Bdgm ($Mg_{0.9}Fe_{0.1}SiO_3$) (Goncharov et al., 2009), and Fp ($Mg_{0.85}Fe_{0.15}O$) (Goncharov et al., 2009). As revealed in this study, the use of 300 K Ppv absorption coefficients underestimates k_{rad} by ~7% at CMB conditions ($P \sim 135$ GPa and $T \sim 4000$ K), assuming that the decrease of the absorption coefficient in the visible range is minor at $T > 2050$ K. At higher temperatures, however, other absorption mechanisms may come into play in the visible range, such as the thermal enhancement of the Fe-O CT band (Lobanov et al., 2016).

To address the effect of iron substitution on radiative conductivity, we applied the 7% correction determined in this work to k_{rad} values inferred from the 300 K absorption data of Ppv with variable iron content (10–30%) reported by Goncharov et al. (2010) (Fig. 3, inset), assuming that iron-depleted Ppv exhibits a similar temperature-dependence of the absorption coefficient. Given the similarities in iron valence and spin distribution between the A- and B-sites in the structures of Bdgm and Ppv (Hsu et al., 2012; Yu et al., 2012), one may expect that the light absorption mechanisms in Bdgm have an analogous temperature-dependence to that in Ppv. Accordingly, we applied the same 7% upward correction to Bdgm radiative conductivity.

Fig. 3 shows a model of the radiative thermal conductivity in the lowermost mantle assuming a ~7 K/km temperature gradient, CMB temperature of 3950 K, and 10% iron in Bdgm and Ppv (Stacey and Davis, 2008). According to the model, the abil-
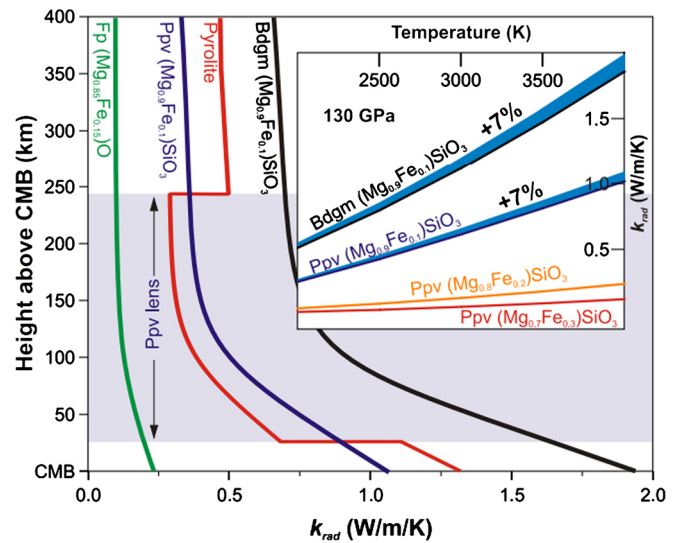
ity of Ppv to conduct heat by radiation is ~ 50% lower than that of Bdgm with a similar composition at expected CMB conditions. The radiative conductivity of Ppv increases from ~0.35 at ~400 km above CMB to 1.1 W/m/K at CMB. Over the same depth interval, Bdgm k_{rad} increases from 0.65 to ~1.95 W/m/K, while in Fp k_{rad} is <0.25 W/m/K, a much lower value than that of Ppv and Bdgm. We note, however, that lower mantle Bdgm and Ppv may have a higher Fe^{3+} content than samples used here (e.g. Sinmyo et al., 2006). Enrichment in Fe^{3+} would inevitably lower radiative thermal conductivity of Bdgm and Ppv due to the intensified Fe^{2+}–Fe^{3+} CT band in the visible range. Radiative conductivity of Ppv, Bdgm, and Fp at CMB conditions is lower than the lattice thermal conductivity of their iron-free counterparts: 15.9 W/m/K (Ppv), 8.6 W/m/K (Bdgm), ~20 W/m/K (periclase) at corresponding conditions, according to experimental measurements using the thermoreflectance method (Dalton et al., 2013; Ohta et al., 2012).

Combining the radiative conductivity model (Fig. 3) with the previously reported k_{lat} values of iron-free Bdgm and iron-free Ppv, we have constrained the total thermal conductivity of a pyrolitic mantle at near CMB conditions to 10.4 and 16.7 W/m/K for Bdgm- and Ppv-dominated rock, respectively. These values, however, are upper bounds on the thermal conductivity because the substitution of iron and/or aluminum in Ppv and Bdgm would inevitably decrease their k_{lat} by 10–50% due to the phonon scattering effects (Ammann et al., 2014; Dalton et al., 2013; Goncharov et al., 2009, 2015; Hsieh et al., 2017; Manthilake et al., 2011;

Okuda et al., 2017; Stackhouse et al., 2015). Accordingly, the total thermal conductivities of individual phases are

$$k_{total}^{Ppv} = \omega * k_{lat}^{\text{Fe-free Ppv}} + k_{rad}^{Ppv} \tag{2}$$

$$k_{total}^{Bdgm} = \omega * k_{lat}^{\text{Fe-free Bdgm}} + k_{rad}^{Bdgm} \tag{3}$$

$$k_{total}^{Fp} = \omega * k_{lat}^{\text{Periclase}} + k_{rad}^{Fp} \tag{4}$$

where ω is the downward correction factor for k_{lat} due to the impurity-induced phonon scattering which must be present in pyrolite. Then the total thermal conductivity of the pyrolitic mantle is:

$$k_{total}^{Pyrolite} = z * \langle k_{total}^{Ppv} + k_{total}^{Fp} \rangle + (1-z) * \langle k_{total}^{Bdgm} + k_{total}^{Fp} \rangle \tag{5}$$

where $\langle \rangle$ brackets denote the Hashin–Shtrikman averaging (Supplementary Materials) (Hashin and Shtrikman, 1962) used to derive the effective conductivity of the mixture of Ppv/Bdgm and Fp in the 4/1 proportion, and z is the abundance of Ppv, $z = \frac{V^{Ppv}}{V^{Ppv}+V^{Bdgm}}$, where V^{Ppv} and V^{Bdgm} are the volumetric fractions of Ppv and Bdgm, respectively. In a hot non-transparent material, such as the lower mantle, the length scale for phonon scattering or photon absorption is much smaller than the grain size (e.g. Keppler et al., 2008). Accordingly, we applied the Hashin–Shtrikman averaging (Hashin and Shtrikman, 1962) in Eqn. (5) in order to model the thermal conductivity of pyrolitic mantle in the TBL. The Hashin–Shtrikman approach proved adequate in determining the effective thermal conductivity of two-phase composites in the absence of detailed information on the spatial distribution of the phases (Hashin and Shtrikman, 1962).

Seismic data suggests that the distribution of Ppv in the lowermost mantle is highly non-uniform, with Ppv concentrated in large (up to 2000 km wide and $\sim$ 200 km thick) lens-shaped structures, as revealed by the abrupt S-wave velocity increase of a few percent (Hernlund and McNamara, 2015; Lay et al., 2006; van der Hilst et al., 2007). However, the global abundance and lateral variations in Ppv content are largely unconstrained. At the same time, it has been proposed that the pressure range of the Bdgm-Ppv transition is inconsistent with the depth of the D" seismic discontinuity, questioning the presence of Ppv in the lowermost mantle (Catalli et al., 2009; Grocholski et al., 2012). It is thus of great interest for the geoscience community to constrain the abundance of Ppv in the TBL in order to evaluate the geodynamic consequences of the Bdgm-Ppv phase transition and the associated increase in the heat flow out of the core (Q_{CMB}) (Hernlund et al., 2005; Lay et al., 2006; van der Hilst et al., 2007).

Geodynamic modeling of the mantle and core has provided an estimate of $Q_{CMB} = 13 \pm 3$ TW (Hernlund and McNamara, 2015; Wu et al., 2011), which is related to the temperature gradient and thermal conductivity of the TBL by the Fourier law of heat conduction:

$$Q_{CMB} = A_{CMB} * k_{total}^{Pyrolite} * \Delta T \tag{6}$$

where A_{CMB} is the surface area of the CMB and ΔT is the temperature gradient above the CMB. Substituting Eqn. (5) for $k_{total}^{Pyrolite}$ in Eqn. (6) and assuming an average temperature gradient of 7 K/km (Stacey and Davis, 2008) we can model the amount of Ppv in a pyrolitic mantle required to sustain the present-day Q_{CMB} as a function of the downward correction factor (ω) to the lattice thermal conductivity (Fig. 4). The values of the thermal conductivity for Ppv, Bdgm, and Fp used in our model are given in the Supplementary Table S1.

Our model suggests that Ppv should be abundant in the lowermost mantle to sustain 13 TW of the present-day CMB heat flow.
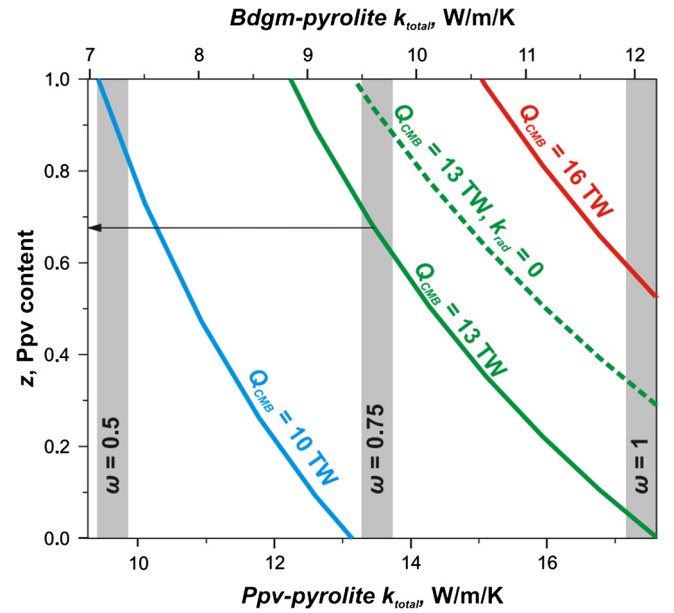

Fig. 4. Ppv content in the thermal boundary layer (TBL) required to sustain the CMB heat flow of 10, 13, and 16 TW (blue, green, and red, respectively) for a given downward correction factor in the lattice conductivity ($\omega \leq 1$) at a temperature gradient of 7 K/km (see text for details). Ppv content (z) is defined as $z = [V_{Ppv}/(V_{Ppv} + V_{Bdgm})]$, where V_{Ppv} and V_{Bdgm} are the volumetric fractions of Ppv and Bdgm, respectively. Black arrow shows the estimation of the Ppv content in the TBL assuming that the correction factor is at 25% according to experiments (Hsieh et al., 2017; Okuda et al., 2017) and molecular dynamic simulations (Ammann et al., 2014; Stackhouse et al., 2015) and $Q_{CMB} = 13$ TW. Dashed green curve shows Ppv content for a model with $k_{rad} = 0$ and $Q_{CMB} = 13$ TW. (For interpretation of the references to color in this figure, the reader is referred to the web version of this article.)

For instance, a modest downward correction in the lattice thermal conductivity ($\omega = 0.75$) for the pyrolitic model requires that Ppv covers $\sim$ 70% of the CMB area (Fig. 4). However, the effect of impurities on the lattice conductivity may be different for Ppv, Bdgm, and Fp. For instance, thermoreflectance data on Fp suggests $\omega < 0.5$ (Ohta et al., 2017) while experiments and molecular dynamic simulations on Bdgm and Ppv point toward more modest corrections ($\omega \sim 0.5$–0.8) (Ammann et al., 2014; Okuda et al., 2017; Stackhouse et al., 2015). In the future, studies of the impurity-retarded lattice thermal conductivity will help to clarify this issue improving our understanding of the feedback between mineralogy, composition, and CMB heat flow. Please note that although the chemical composition of the lowermost mantle is unknown, higher Fe content (greater than assumed 10 mol.% Fe) would further reduce both k_{rad} and k_{lat}. As a result, more Ppv phase would be needed to sustain the CMB heat flow (see $k_{rad} = 0$ model in Fig. 4). In fact, this underscores the importance of radiative heat transport in maintaining the balance among mineral phases, their composition, and heat flow. The inferred abundance of Ppv is based on a model that does not rely on the highly uncertain parameters such as the depth and Clapeyron slope of the Bdgm–Ppv transition. Nonetheless, the derived volume ratio of Bdgm/Ppv is consistent with the value (Bdgm/Ppv $\sim$1) derived from the analysis of the D" seismic discontinuity in the region (Houser, 2007). The presence of such large portions of Ppv with relatively high lattice thermal conductivity (as compared to Bdgm) (Ammann et al., 2014; Haigis et al., 2012; Ohta et al., 2012) at the base of the lower mantle would result in mantle temperatures up to 500 K higher than that in a Ppv-free lowermost mantle, decreasing the buoyancy of plumes (Tosi et al., 2013). Likewise, higher temperatures will reduce mantle viscosity amplifying the vigor of whole mantle convection and triggering small-scale convection in the TBL (Samuel and Tosi, 2012). If the lowermost mantle is enriched in

iron, the downward correction in k_{lat} may be as large as 0.5 (Dalton et al., 2013; Goncharov et al., 2015; Hsieh et al., 2017; Manthilake et al., 2011), in which case the TBL must be dominated by Ppv even for the Q_{CMB} of 10 TW. On the other hand, $Q_{CMB} > 16$ TW demand that the whole TBL region is dominated by Ppv even for $\omega = 1$. However, the $Q_{CMB} < 10$ TW and $Q_{CMB} > 16$ TW scenarios are unlikely because they contradict mineral physics data on the impurity-dependence of lattice thermal conductivity of lower mantle minerals (Ammann et al., 2014; Dalton et al., 2013; Manthilake et al., 2011; Stackhouse et al., 2015). Overall, our models show that most recent estimates of $Q_{CMB} = 13 \pm 3$ TW (Hernlund and McNamara, 2015; Wu et al., 2011) are consistent with the Ppv interpretation of the D" seismic discontinuity. Future experimental and theoretical studies on the impurities effects on k_{lat} will enhance our understanding of the mineralogy and dynamical consequences of the Bdgm–Ppv phase transition of the CMB region.

Acknowledgements

Appendix A. Supplementary material

Supplementary material related to this article can be found online at http://dx.doi.org/10.1016/j.epsl.2017.09.016.

References

Ammann, M.W., Walker, A.M., Stackhouse, S., Wookey, J., Forte, A.M., Brodholt, J.P., Dobson, D.P., 2014. Variation of thermal conductivity and heat flux at the Earth's core mantle boundary. Earth Planet. Sci. Lett. 390, 175–185.

Burns, R.G., 1993. Mineralogical Applications of Crystal Field Theory, 2nd ed. Cambridge University Press, UK.

Catalli, K., Shim, S.H., Prakapenka, V., 2009. Thickness and Clapeyron slope of the post-perovskite boundary. Nature 462, 782–785.

Cox, P.A., 1980. Electron transfer between exchange-coupled ions in a mixed-valency compound. Chem. Phys. Lett. 69, 340–343.

Dalton, D.A., Hsieh, W.P., Hohensee, G.T., Cahill, D.G., Goncharov, A.F., 2013. Effect of mass disorder on the lattice thermal conductivity of MgO periclase under pressure. Sci. Rep. 3, 02400.

Ferguson, J., Guggenheim, H.J., Tanabe, Y., 1965. Absorption of light by pairs of like and unlike transition-metal ions. Phys. Rev. Lett. 14, 737–738.

Goncharov, A.F., Beck, P., Struzhkin, V.V., Haugen, B.D., Jacobsen, S.D., 2009. Thermal conductivity of lower-mantle minerals. Phys. Earth Planet. Inter. 174, 24–32.

Goncharov, A.F., Haugen, B.D., Struzhkin, V.V., Beck, P., Jacobsen, S.D., 2008. Radiative conductivity in the Earth's lower mantle. Nature 456, 231–234.

Goncharov, A.F., Lobanov, S.S., Tan, X., Hohensee, G.T., Cahill, D.G., Lin, J.F., Thomas, S.M., Okuchi, T., Tomioka, N., 2015. Experimental study of thermal conductivity at high pressures: implications for the deep Earth's interior. Phys. Earth Planet. Inter. 247, 11–16.

Goncharov, A.F., Struzhkin, V.V., Jacobsen, S.D., 2006. Reduced radiative conductivity of low-spin (Mg, Fe)O in the lower mantle. Science 312, 1205–1208.

Goncharov, A.F., Struzhkin, V.V., Montoya, J.A., Kharlamova, S., Kundargi, R., Siebert, J., Badro, J., Antonangeli, D., Ryerson, F.J., Mao, W., 2010. Effect of composition, structure, and spin state on the thermal conductivity of the Earth's lower mantle. Phys. Earth Planet. Inter. 180, 148–153.

Grocholski, B., Catalli, K., Shim, S.H., Prakapenka, V., 2012. Mineralogical effects on the detectability of the postperovskite boundary. Proc. Natl. Acad. Sci. USA 109, 2275–2279.

Haigis, V., Salanne, M., Jahn, S., 2012. Thermal conductivity of MgO, MgSiO₃ perovskite and post-perovskite in the Earth's deep mantle. Earth Planet. Sci. Lett. 355, 102–108.

Hashin, Z., Shtrikman, S., 1962. A variational approach to theory of effective magnetic permeability of multiphase materials. J. Appl. Phys. 33, 3125–3131.

Hernlund, J.W., McNamara, A.K., 2015. The core–mantle boundary region A2. In: Schubert, Gerald (Ed.), Treatise on Geophysics, 2nd ed. Elsevier, Oxford, pp. 461–519. Chapter 7.11.

Hernlund, J.W., Thomas, C., Tackley, P.J., 2005. A doubling of the post-perovskite phase boundary and structure of the Earth's lowermost mantle. Nature 434, 882–886.

Hofmeister, A.M., 2014. Thermodynamic and optical thickness corrections to diffusive radiative transfer formulations with application to planetary interiors. Geophys. Res. Lett. 41, 3074–3080.

Holmstrom, E., Stixrude, L., 2015. Spin crossover in ferropericlase from first-principles molecular dynamics. Phys. Rev. Lett. 114, 117202.

Houser, C., 2007. Constraints on the presence or absence of post-perovskite in the lowermost mantle from long-period seismology. In: Hirose, K., Brodholt, J., Lay, T., Yuen, D. (Eds.), Geophys. Monogr. Ser., pp. 191–216.

Hsieh, W.-P., Deschamps, F., Okuchi, T., Lin, J.-F., 2017. Reduced lattice thermal conductivity of Fe-bearing bridgmanite in Earth's deep mantle. J. Geophys. Res., Solid Earth 122.

Hsu, H., Yu, Y.G.G., Wentzcovitch, R.M., 2012. Spin crossover of iron in aluminous MgSiO₃ perovskite and post-perovskite. Earth Planet. Sci. Lett. 359, 34–39.

Ismailova, L., Bykova, E., Bykov, M., Cerantola, V., McCammon, C., Boffa Ballaran, T., Bobrov, A., Sinmyo, R., Dubrovinskaia, N., Glazyrin, K., Liermann, H.-P., Kupenko, I., Hanfland, M., Prescher, C., Prakapenka, V., Svitlyk, V., Dubrovinsky, L., 2016. Stability of Fe, Al-bearing bridgmanite in the lower mantle and synthesis of pure Fe-bridgmanite. Sci. Adv. 2, e1600427.

Keppler, H., Dubrovinsky, L.S., Narygina, O., Kantor, I., 2008. Optical absorption and radiative thermal conductivity of silicate perovskite to 125 Gigapascals. Science 322, 1529–1532.

Keppler, H., Kantor, I., Dubrovinsky, L.S., 2007. Optical absorption spectra of ferropericlase to 84 GPa. Am. Mineral. 92, 433–436.

Lay, T., Hernlund, J., Buffett, B.A., 2008. Core–mantle boundary heat flow. Nat. Geosci. 1, 25–32.

Lay, T., Hernlund, J., Garnero, E.J., Thorne, M.S., 2006. A post-perovskite lens and D″ heat flux beneath the central Pacific. Science 314, 1272–1276.

Lin, J.-F., Mao, Z., Yang, J., Liu, J., Xiao, Y., Chow, P., Okuchi, T., 2016. High-spin Fe²⁺ and Fe³⁺ in single-crystal aluminous bridgmanite in the lower mantle. Geophys. Res. Lett., 6952–6959.

Lin, J.F., Watson, H., Vanko, G., Alp, E.E., Prakapenka, V.B., Dera, P., Struzhkin, V.V., Kubo, A., Zhao, J.Y., McCammon, C., Evans, W.J., 2008. Intermediate-spin ferrous iron in lowermost mantle post-perovskite and perovskite. Nat. Geosci. 1, 688–691.

Lobanov, S.S., Goncharov, A.F., Litasov, K.D., 2015. Optical properties of siderite (FeCO₃) across the spin transition: crossover to iron-rich carbonates in the lower mantle. Am. Mineral. 100, 1059–1064.

Lobanov, S.S., Holtgrewe, N., Goncharov, A.F., 2016. Reduced radiative conductivity of low spin FeO₆-octahedra in FeCO₃ at high pressure and temperature. Earth Planet. Sci. Lett. 449, 20–25.

Lobanov, S.S., Hsu, H., Lin, J.F., Yoshino, T., Goncharov, A.F., 2017. Optical signatures of low spin Fe³⁺ in NAL at high pressure. J. Geophys. Res., Solid Earth 122, 3565–3573.

Manthilake, G.M., de Koker, N., Frost, D.J., McCammon, C.A., 2011. Lattice thermal conductivity of lower mantle minerals and heat flux from Earth's core. Proc. Natl. Acad. Sci. USA 108, 17901–17904.

Mattson, S.M., Rossman, G.R., 1987. Identifying characteristics of charge transfer transitions in minerals. Phys. Chem. Miner. 14, 94–99.

Murakami, M., Hirose, K., Kawamura, K., Sata, N., Ohishi, Y., 2004. Post-perovskite phase transition in MgSiO₃. Science 304, 855–858.

Oganov, A.R., Ono, S., 2004. Theoretical and experimental evidence for a post-perovskite phase of MgSiO₃ in Earth's D″ layer. Nature 430, 445–448.

Ohta, K., Yagi, T., Hirose, K., Ohishi, Y., 2017. Thermal conductivity of ferropericlase in the Earth's lower mantle. Earth Planet. Sci. Lett. 465, 29–37.

Ohta, K., Yagi, T., Taketoshi, N., Hirose, K., Kornabayashi, T., Baba, T., Ohishi, Y., Hernlund, J., 2012. Lattice thermal conductivity of $MgSiO_3$ perovskite and post-perovskite at the core–mantle boundary. Earth Planet. Sci. Lett. 349, 109–115.

Okuda, Y., Ohta, K., Yagi, T., Sinmyo, R., Wakamatsu, T., Hirose, K., Ohishi, Y., 2017. The effect of iron and aluminum incorporation on lattice thermal conductivity of bridgmanite at the Earth's lower mantle. Earth Planet. Sci. Lett. 474, 25–31.

Ruf, T., Cardona, M., Pickles, C.S.J., Sussmann, R., 2000. Temperature dependence of the refractive index of diamond up to 925 K. Phys. Rev. B 62, 16578–16581.

Samuel, H., Tosi, N., 2012. The influence of post-perovskite strength on the Earth's mantle thermal and chemical evolution. Earth Planet. Sci. Lett. 323, 50–59.

Sherman, D.M., 1987. Molecular orbital (SCF-Xα-SW) theory of metal–metal charge transfer processes in minerals. I Application to $Fe^{2+} \rightarrow Fe^{3+}$ charge transfer and "electron delocalization" in mixed-valence iron oxides and silicates. Phys. Chem. Miner. 14, 355–363.

Sinmyo, R., Hirose, K., O'Neill, H.S., Okunishi, E., 2006. Ferric iron in Al-bearing post-perovskite. Geophys. Res. Lett. 33, L12S13.

Stacey, F.D., Davis, P.M., 2008. Physics of the Earth, 4th ed. Cambridge University Press, Cambridge, New York.

Stackhouse, S., Stixrude, L., Karki, B.B., 2015. First-principles calculations of the lattice thermal conductivity of the lower mantle. Earth Planet. Sci. Lett. 427, 11–17.

Thomas, S.M., Bina, C.R., Jacobsen, S.D., Goncharov, A.F., 2012. Radiative heat transfer in a hydrous mantle transition zone. Earth Planet. Sci. Lett. 357, 130–136.

Tosi, N., Yuen, D.A., de Koker, N., Wentzcovitch, R.M., 2013. Mantle dynamics with pressure- and temperature-dependent thermal expansivity and conductivity. Phys. Earth Planet. Inter. 217, 48–58.

van der Hilst, R.D., de Hoop, M.V., Wang, P., Shim, S.H., Ma, P., Tenorio, L., 2007. Seismostratigraphy and thermal structure of Earth's core–mantle boundary region. Science 315, 1813–1817.

Wall, A., Price, G.D., Parker, S.C., 1986. A computer simulation of the structure and elastic properties of $MgSiO_3$ perovskite. Mineral. Mag. 50, 693–707.

Wu, B.J., Driscoll, P., Olson, P., 2011. A statistical boundary layer model for the mantle D'' region. J. Geophys. Res., Solid Earth 116.

Yu, Y.G.G., Hsu, H., Cococcioni, M., Wentzcovitch, R.M., 2012. Spin states and hyperfine interactions of iron incorporated in $MgSiO_3$ post-perovskite. Earth Planet. Sci. Lett. 331, 1–7.